

Article

Influence of the Addition of Ni on as-Cast Microstructure of Duplex Fe-Mn-Al-C Lightweight Steel

Jaka Burja ^{1,2,*} , Barbara Šetina Batič ¹ and Tilen Balaško ² 

¹ Institute of Metals and Technology, Metallic Materials and Technology, 1000 Ljubljana, Slovenia; barbara.setina@imt.si

² Faculty of Natural Sciences and Engineering, University of Ljubljana, 1000 Ljubljana, Slovenia; tilen.balasko@ntf.uni-lj.si

* Correspondence: jaka.burja@imt.si; Tel.: +386-14701981

Abstract: Lightweight Fe-Mn-Al-C steels have low density, and high mechanical properties, which makes them a possibility for weight reduction in vehicles for road transport. In steel production, as-cast microstructure is an important parameter for further processing. The as-cast microstructure of five lightweight duplex steels was investigated: Fe-15Mn-10Al-0.8C, Fe-15Mn-10Al-1.7Ni-0.8C, Fe-15Mn-10Al-3.9Ni-0.8C, Fe-15Mn-10Al-5.6Ni-0.8C and Fe-15Mn-10Al-8.6Ni-0.8C. The influence of Ni was analysed through thermodynamic calculations and microstructural characterization. The samples were analysed through an optical and electron microscopy. The base microstructure of the studied steel consists of ferrite and austenite. Further investigation showed that the decomposition of austenite was accompanied by the formation of kappa carbides and the B2 ordered phase. The addition of Ni prevented the formation of a lamellar kappa ferrite morphology, but at 5.6 wt.% Ni, the decomposition of austenite was most severe, resulting in a large amount of kappa carbides and a B2 ordered phase.



Citation: Burja, J.; Šetina Batič, B.; Balaško, T. Influence of the Addition of Ni on as-Cast Microstructure of Duplex Fe-Mn-Al-C Lightweight Steel. *Crystals* **2021**, *11*, 1551. <https://doi.org/10.3390/cryst11121551>

Academic Editor: José L. García

Received: 12 November 2021

Accepted: 9 December 2021

Published: 11 December 2021

Publisher's Note: MDPI stays neutral with regard to jurisdictional claims in published maps and institutional affiliations.



Copyright: © 2021 by the authors. Licensee MDPI, Basel, Switzerland. This article is an open access article distributed under the terms and conditions of the Creative Commons Attribution (CC BY) license (<https://creativecommons.org/licenses/by/4.0/>).

Keywords: duplex steel; lightweight steel; microstructure; Fe-Mn-Al-C steel; kappa carbides

1. Introduction

In the European Union (EU), about 20% of greenhouse gas (GHG) emissions come from transport, with road transport responsible for about 72% [1–3]. Of these, passenger cars and vans (light-duty vehicles) account for around 15% of CO₂ emissions in the EU's [4]. Therefore, reducing CO₂ emissions by minimising vehicle mass [3–5] is an important aspect for sustainable transport. Mass reduction is the main driving force for the development of Fe-Mn-Al-C steels for automotive applications [6–8]. The matrix phase of lightweight steels can be ferritic, austenitic, or duplex (ferritic and austenitic) depending on the chemical composition, mainly Al, C, and Mn [6,9–12]. The Fe-Mn-Al-C steels have high strength and low density, with the density decreasing by 1.3% with each wt.% of Al [13–15]. However, the high Al content also promotes the formation of a B2 ordered phase and nano-sized kappa carbides (κ). The formation of the aforementioned phases increases the mechanical properties, namely tensile strength and hardness through the precipitation hardening mechanism. The addition of Ni to the Fe-Mn-Al-C steel system can promote the precipitation of the B2 ordered phase in the γ -austenite matrix (FCC) [16–21]. The B2 ordered phase also increases corrosion resistance [22]. The addition of Ni is widely used in stainless steels to promote the γ -austenite region, especially in austenitic and duplex stainless steels [23,24]. The addition of 8 wt.% Ni provides a fully austenitic microstructure after heat treatment. The effect on Fe-Mn-Al-C lightweight steels is somewhat different and is the subject of this article. The as-cast microstructure of steels is important for applications in castings as well as for further processing of ingots, billets, slabs, etc. The as-cast microstructure can cause cracks, prove difficult to machine and dictates the regime of further annealing due to the dissolution of different phases. The formation of different phases in the microstructure of

five different Fe-15Mn-10Al-0.8C-XNi steels with different Ni contents (0, 1.7, 3.9, 5.6 and 8.6 wt.%) was investigated.

2. Materials and Methods

A total of 10 kg of steel was melted in a vacuum induction melting furnace under a 300-mbar argon protective atmosphere. Pure elements, Al, Mn, Ni, and C and mild steel were used to produce the steel. The steels were cast into a 210 mm long ingot, which was 80 mm wide at the bottom and 90 mm wide at the top.

The chemical composition (Table 1) was measured by a wet chemical analysis and infrared absorption after combustion with ELTRA CS-800 (ELTRA GmbH, Haan, Germany). The samples were then prepared for metallographic analysis by grinding and polishing. For microstructural observations, the samples were etched in 10% Nital and for electron backscattered diffraction measurements the polished samples were additionally polished with oxide polishing suspension (OPS) for 5 min.

Table 1. Chemical composition of samples is expressed in percent by weight.

Sample	C	Si	Cu	Ni	Mn	Al	Fe
FeMnAlC	0.81	0.20	0.17	0.1	15.0	10.0	Balance
FeMnAl1.7NiC	0.81	0.21	0.17	1.7	14.9	10.2	Balance
FeMnAl3.9NiC	0.83	0.19	0.17	3.9	14.8	10.0	Balance
FeMnAl5.6NiC	0.82	0.20	0.17	5.6	14.8	10.1	Balance
FeMnAl8.6NiC	0.83	0.19	0.16	8.6	14.7	10.1	Balance

Microstructural characterization was performed through an optical microscope Microphot FXA, Nikon (Nikon, Minato City, Japan) with a 3CCD video camera Hitachi HV-C20A (Hitachi, Ltd., Tokyo, Japan) and a scanning electron microscope JEOL JSM 6450-F (Jeol, Tokyo, Japan). An additional microanalysis was performed using an energy dispersive spectroscopy (EDS) (Ultim[®] Max, Oxford Instruments, Abingdon, UK) and electron backscatter diffraction (EBSD) (EDAX, Mahwah NJ, USA).

For CALPHAD calculations, the commercial software Thermo-Calc version 2021b (Thermo-Calc Software AB, Stockholm, Sweden) [25] was used. The Thermo-Calc software TCFE10 Steels/Fe-alloys database was selected to obtain the thermodynamic data for the calculations [26]. We used the Equilibrium Calculator and selected the Property Diagram calculation type, from which we obtained diagrams, showing the characteristic temperatures and the amount of thermodynamically stable phases in the steels studied.

3. Results and Discussion

3.1. CALPHAD Calculations

The CALPHAD calculations (Figure 1) show the amount of thermodynamically stable phases in the steels studied. In Table 2, the characteristic temperatures of the equilibrium phases are provided, i.e., the temperatures of precipitation, transformation, liquidus, and solidus. Ni increases the solidification interval, its influence on solidification was already described in detail in our previous research [27]. The calculation results show that the addition of Ni decreases the liquidus temperature (Table 2) from 1407 °C (FeMnAlC) to 1380 °C (FeMnAl8.6NiC). The same trend is observed in the solidus temperature, which decreases from 1299 °C (FeMnAlC) to 1245 °C (FeMnAl8.6NiC). This means that the liquidus temperature decreased by 27 °C and the solidus temperature decreased by 54 °C. On the other hand, the precipitation temperature of γ -austenite (FCC_A1 in Table 2) decreases from 1340 °C (FeMnAlC) to 1252 °C (FeMnAl8.6NiC) due to the addition of Ni. The same trend is observed in the stability of γ -austenite (FCC_A1_finish in Table 2) in the studied steels, where in the sample without Ni addition (FeMnAlC) γ -austenite is stable up to a temperature of 702 °C and in the sample with 8.6 wt.% Ni addition (FeMnAl8.6NiC) γ -austenite is stable up to a temperature of 436 °C. This means, that the precipitation temperature of γ -austenite (FCC_A1) is decreased by 52 °C and the stability of γ -austenite

(FCC_A1_finish) decreased by 266 °C. The precipitation temperature of δ -ferrite (BCC_A2 in Table 2) is also decreased from 1407 °C (FeMnAlC) to 1380 °C (FeMnAl8.6NiC), but on the other hand, the transformation temperature of δ -ferrite (BCC_A2 in Table 2) to the ordered B2 phase (BCC_B2 in Table 2) is increased from 715 °C (FeMnAlC) to 1247 °C (FeMnAl8.6NiC). This means that the precipitation temperature of δ -ferrite (BCC_B2) decreases for a temperature of 27 °C and, the transformation temperature of δ -ferrite (BCC_A2) to the ordered B2 phase (BCC_B2) increases to 532 °C. The transformation temperature of δ -ferrite (BCC_A2) to the ordered B2 phase (BCC_B2) also affects the starting temperature of the B2 ordered phase transformation, which is 739 °C for the sample without Ni addition (FeMnAlC) and 1248 °C for the sample with an 8.6 wt.% Ni addition (FeMnAl8.6NiC). It can be concluded that the starting temperature of the B2 ordered phase transformation is increased to 509 °C. On the other hand, the precipitation temperature of kappa carbide (KAPPA_E21 in Table 2) decreases from 947 °C (FeMnAlC) to 827 °C (FeMnAl8.6NiC) with the addition of Ni i.e., it decreases by 120 °C. However, when the B2 ordered phase (BCC_B2) is transformed to α -ferrite (BCC_A2 in Table 2), the temperature increases from 564 °C (FeMnAlC) to 661 °C (FeMnAl8.6NiC). It is also evident that the Ni addition affects the transformation sequence of α -ferrite (BCC_A2). For steel without Ni addition, the transformation proceeds from B2 ordered phase (BCC_B2) to α -ferrite (BCC_A2), the higher the Ni addition, the more we approach the transformation from γ -austenite (FCC_A1) to α -ferrite (BCC_A2). With the Ni addition of 8.6 wt.% (Figure 1e), the decrease in the B2 ordered phase (BCC_B2) is minimal, which means that the transformation is almost exclusively from γ -austenite (FCC_A1) to α -ferrite (BCC_A2).

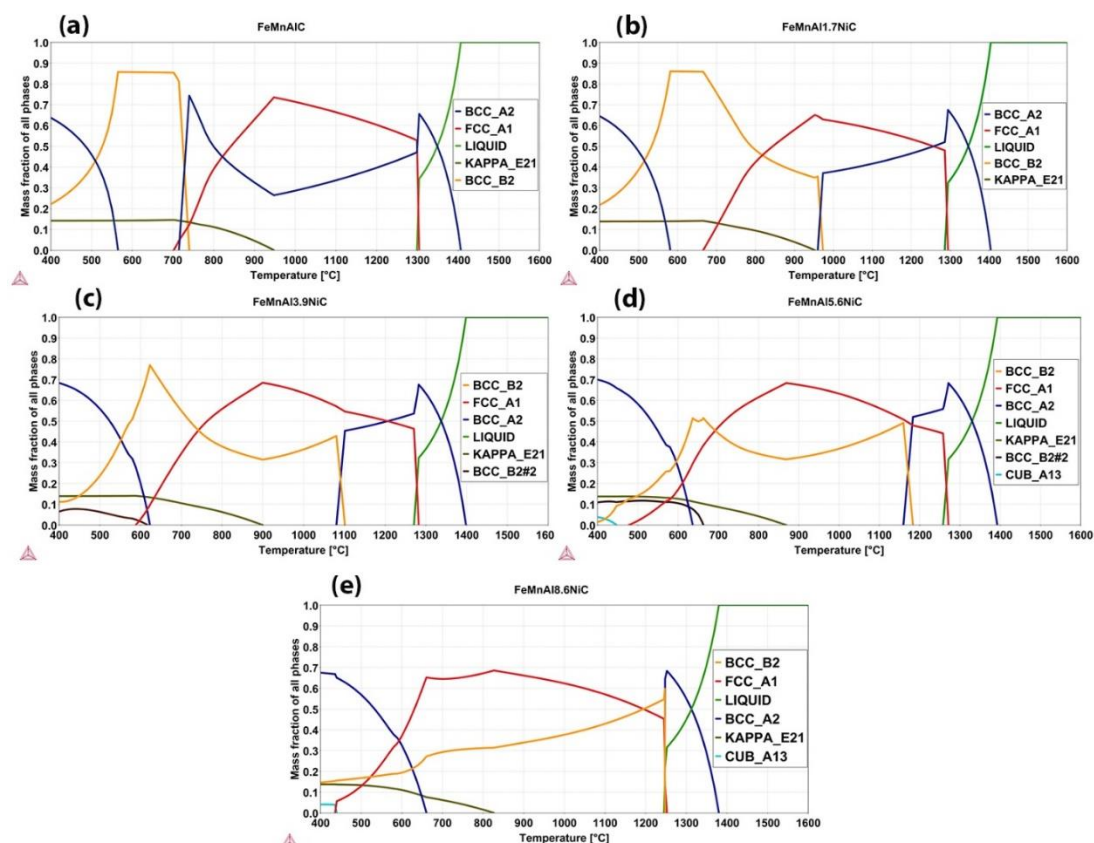


Figure 1. CALPHAD calculations of the equilibrium amount of phases in the steels studied, (a) FeMnAlC, (b) FeMnAl1.7NiC, (c) FeMnAl3.9NiC, (d) FeMnAl5.6NiC, and (e) FeMnAl8.6NiC.

Table 2. Characteristic temperatures of the equilibrium phases.

Sample	Temperature/°C								
	Liquidus	Solidus	FCC_A1	FCC_A1_finish	BCC_A2	BCC_A2_finish	BCC_B2	Kappa	BCC_A2
FeMnAlC	1407	1299	1304	702	1407	715	739	947	564
FeMnAl1.7NiC	1404	1286	1294	666	1404	960	973	952	581
FeMnAl3.9NiC	1398	1271	1282	588	1398	1080	1101	899	623
FeMnAl5.6NiC	1393	1258	1271	478	1393	1159	1183	868	636
FeMnAl8.6NiC	1380	1245	1252	436	1380	1247	1248	827	661

3.2. Optical Microscopy

The microstructure of the as-cast samples appears to consist of two phases, an α -ferrite, and a γ -austenite phase with precipitated kappa carbides. The lighter phase is α -ferrite, and the darker phase is γ -austenite (Figure 2). The dendritic morphology of α -ferrite shows a typical as-cast microstructure. The carbides at the ferrite/austenite grain boundaries are coarser and needle shaped in the sample without Ni addition (FeMnAlC). Lower additions of Ni, FeMnAl1.7NiC and FeMnAl3.9NiC seem to promote the formation of finer round carbides. However, higher additions of Ni, FeMnAl5.6NiC, promote the precipitation of very fine carbides within the austenite grains. FeMnAl8.6NiC, on the other hand, shows a similar morphology to the samples with lower additions of Ni (FeMnAl1.7NiC and FeMnAl3.9NiC).

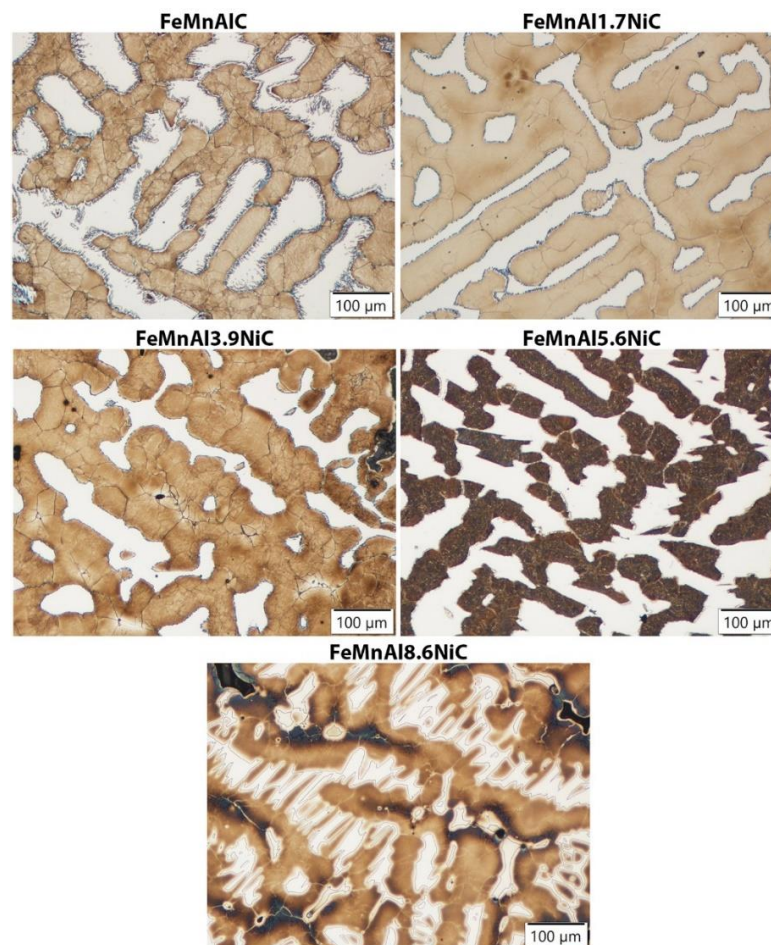


Figure 2. Optical microscopy of Fe-Mn-Al-XNi-C steel as-cast microstructure, with different Ni contents.

3.3. Scanning Electron Microscopy

The SEM EBSD mappings of all samples are shown in Figure 3. The ferrite (BCC) phase is shown as red, while the austenite (FCC) phase is shown as blue. The orientation of each phase is also provided by the inverse pole figures.

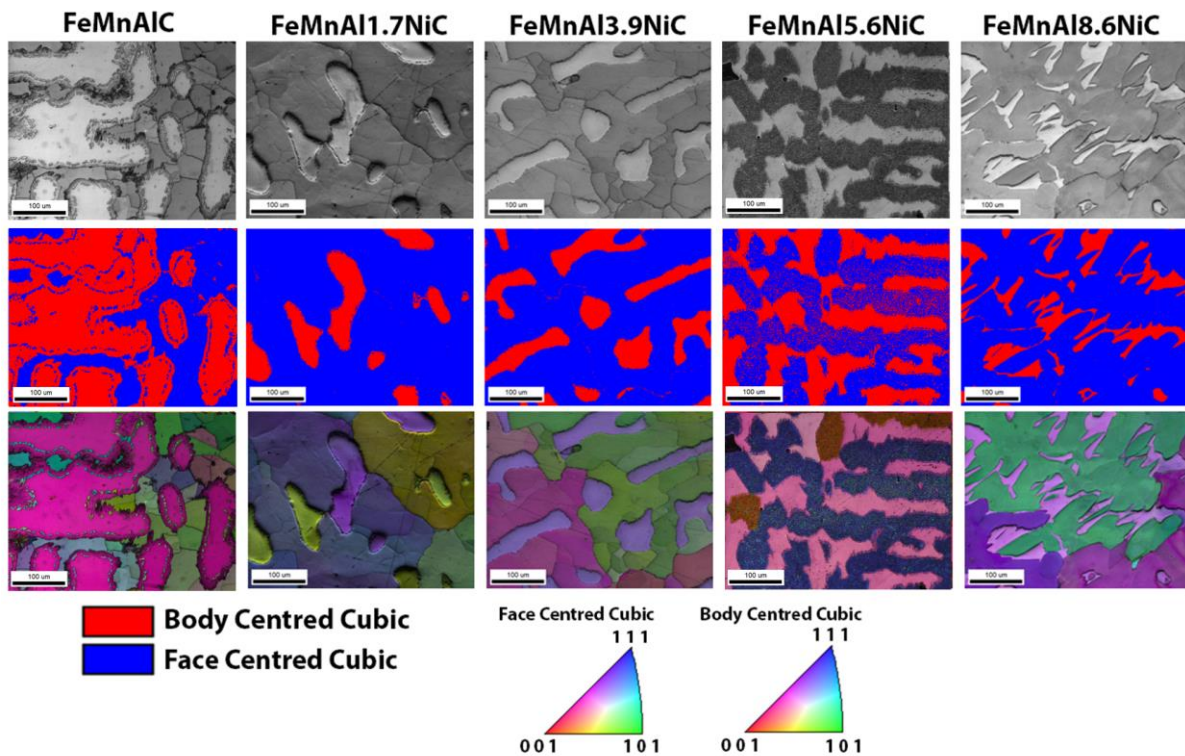


Figure 3. Electron backscattered diffraction analysis of as-cast FeMnAlC samples with different Ni contents.

A lamellar morphology of kappa carbides was observed in the ferrite matrix (Figure 4). These were formed by the $\gamma = \kappa + \alpha$ reaction, and the kappa carbides are $\sim 1 \mu\text{m}$ wide. While the kappa carbides in γ -austenite are in the nanoscale. The kappa carbides formed in γ -austenite are the result of spinodal decomposition [28,29]. However, the lamellar morphology is not observed at every α -ferrite/ γ -austenite phase boundary; in fact, for most interphases this is not the case. The transformation fronts consist of larger grains of FCC phase (face-centred cubic) and smaller grains near the FCC phase (Figure 4). Both the kappa carbides and austenite are characterised as FCC in the EBSD mapping, which is due to the inverse perovskite crystal lattice of the kappa carbides, which is very similar to FCC. However, the enrichment of Mn and Al in the EDS mapping, indicates kappa carbides. Moreover, the kappa carbides and untransformed γ -austenite maintain the same crystal orientation, as shown in Figure 5.

Samples with Ni additions do not show a lamellar morphology of kappa carbides, they show the previously mentioned transformation fronts, where some of the FCC islets are untransformed in the body-centred cubic (BCC) structure. These FCC islets are enriched in Mn and Al, they also maintain the crystal orientation of the parent FCC γ -austenite, as seen in Figures 6 and 7. Some ordering between α -ferrite ($\alpha = \text{B2} + \alpha'$) and γ -austenite ($\gamma = \text{B2} + \kappa + \gamma'$) is visible but not clearly defined, as seen in Figure 5. Small additions of Ni lower the temperatures for the formation of kappa carbides as shown by the thermodynamic calculations in Figure 1. The decreased appearance of kappa carbides is also visible in the microstructures in Figures 6–8.

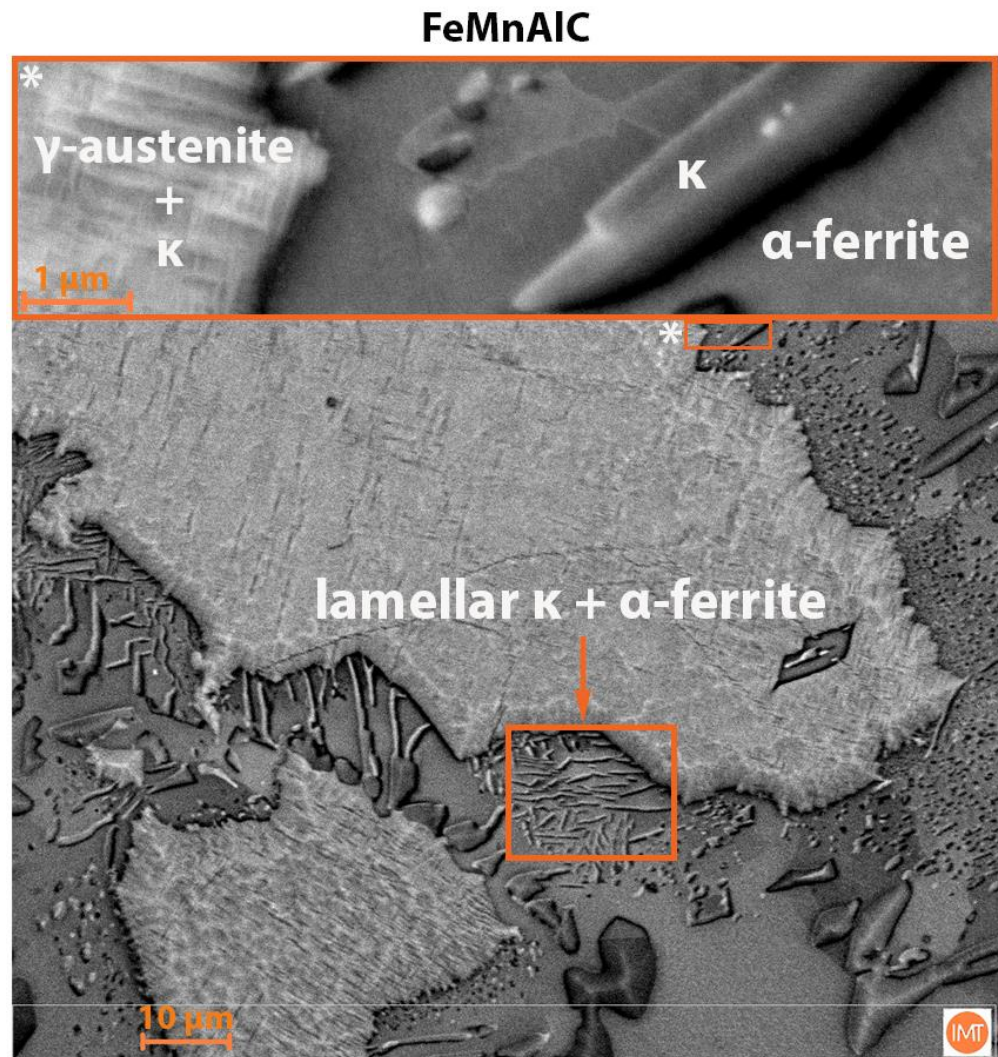


Figure 4. Lamellar morphology of kappa carbides.

The microstructure of the sample with 5.6 wt.% Ni differs from the other samples, as the γ -austenite phase is almost completely decomposed. The SEM analysis shows the B2 ordered phase + kappa carbides and γ -austenite, while the α -ferrite grains remain stable, as can be seen in Figure 9. The closer examination of the former γ -austenite phase is shown in Figure 10. The microstructure of the decomposed γ -austenite consists of kappa carbides, B2 ordered phase and γ -austenite. The kappa carbides in γ -austenite are the result of spinodal decomposition as described by Mapelli et al. and Lu et al. [28,29]. The identification of kappa carbides and the ordered B2 phase can be difficult, but we distinguished them based on microchemical composition. The kappa carbides are richer in Al and Mn, while the B2 ordered phase contains more Ni. The remaining austenite is denser and can be seen as the brighter phase in backscattered electron images.

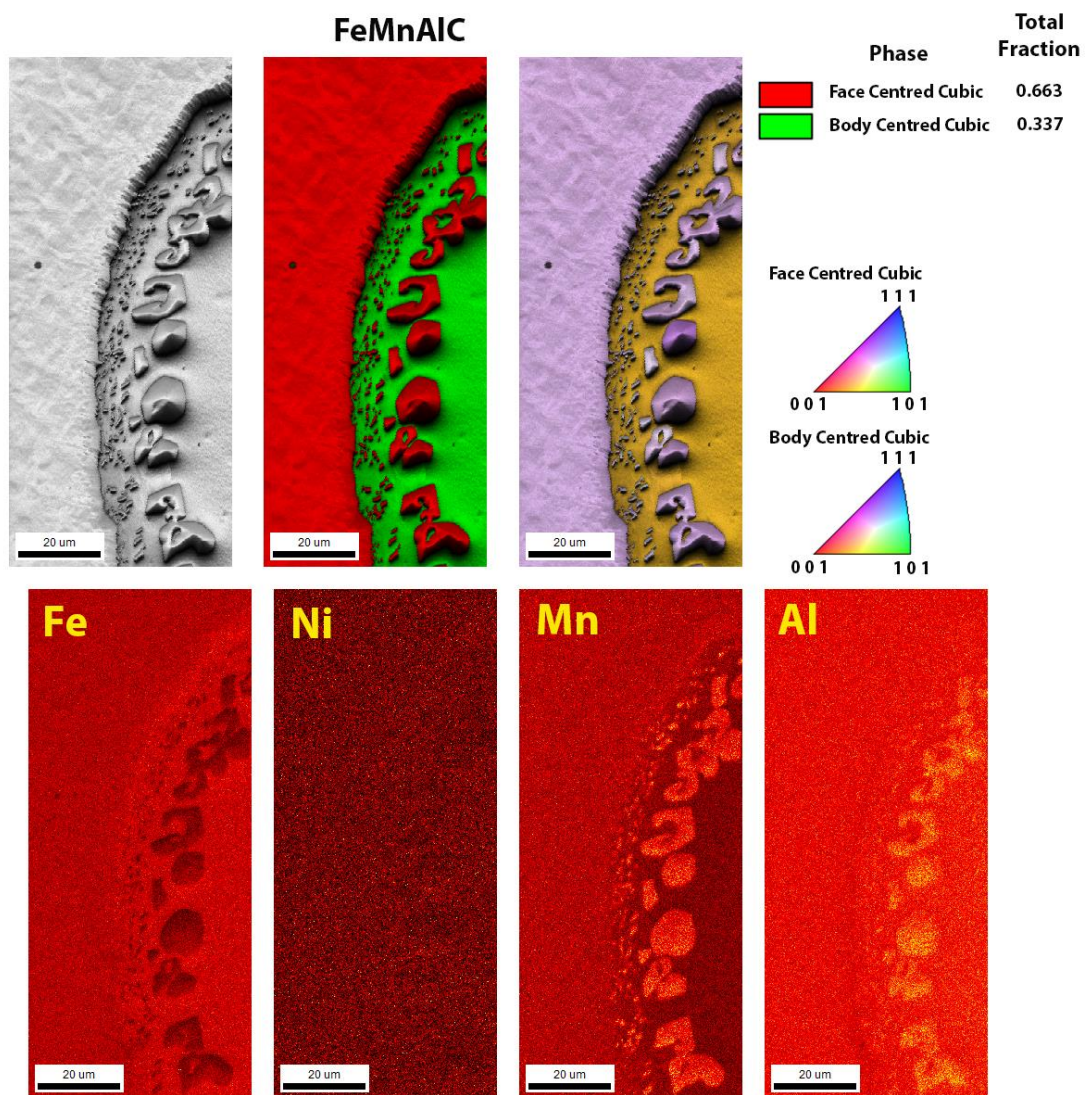


Figure 5. Electron backscattered diffraction analysis of a sample as-cast FeMnAlC sample and SEM EDS (Energy-dispersive X-ray spectroscopy) elemental mapping of Fe, Ni, Mn, and Al.

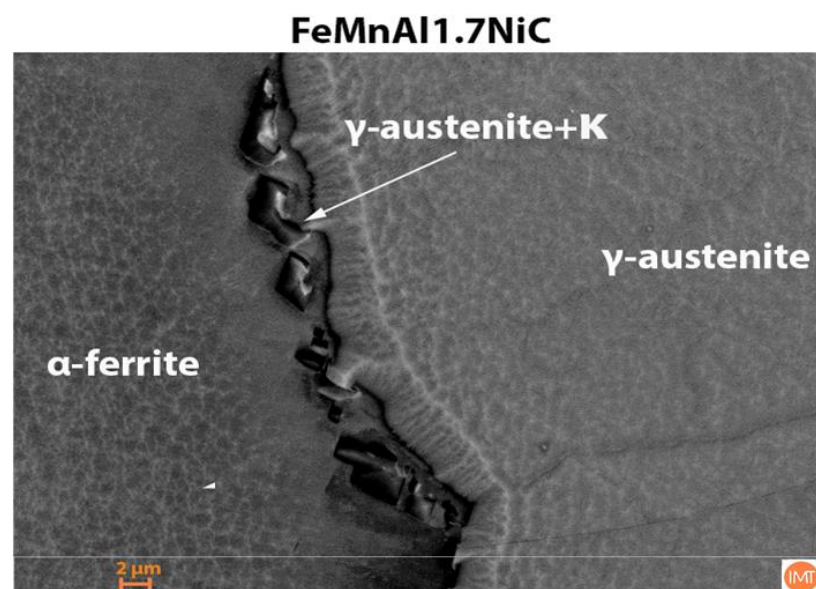


Figure 6. Fe-Mn-Al-1.7Ni-C steel microstructure with the BCC/FCC phase boundary.

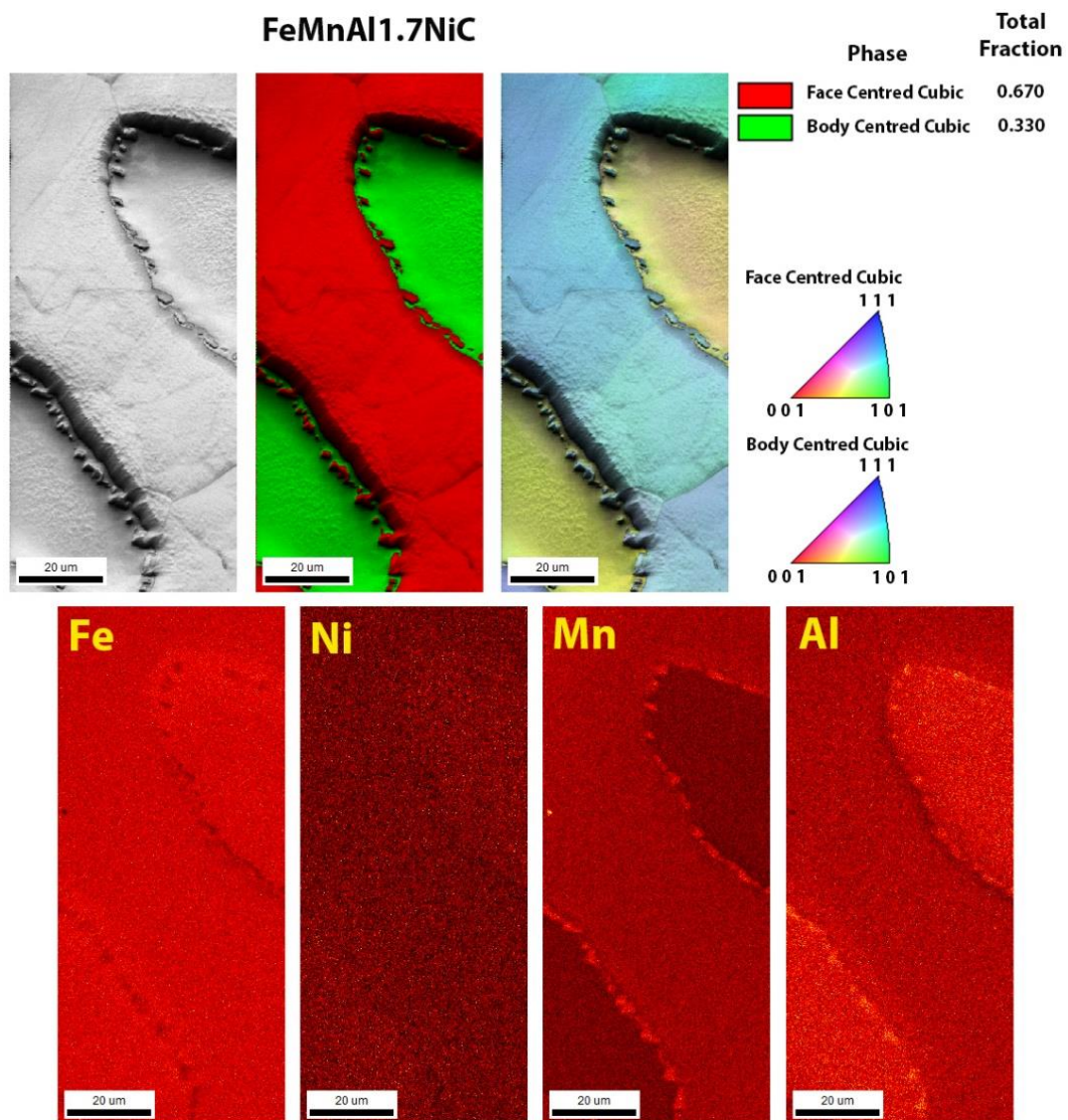


Figure 7. Electron backscattered diffraction analysis of a sample as-cast FeMnAl1.7NiC sample and SEM EDS (Energy-dispersive X-ray spectroscopy) elemental mapping of Fe, Ni, Mn, and Al.

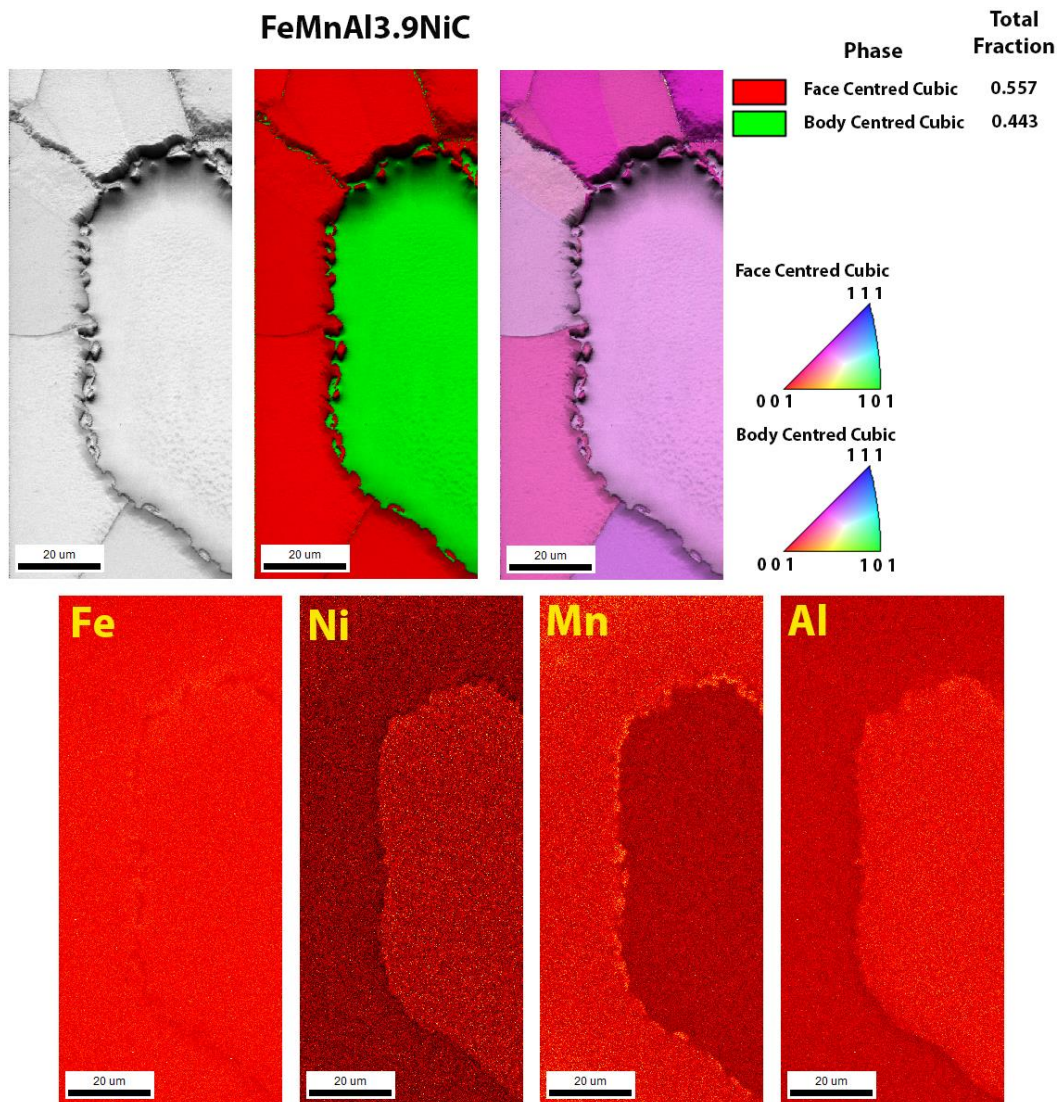


Figure 8. Electron backscattered diffraction analysis of a sample as-cast FeMnAl3.9NiC sample and SEM EDS (Energy-dispersive X-ray spectroscopy) elemental mapping of Fe, Ni, Mn, and Al.

The sample with the highest Ni content (8.6 wt.%) has a simple duplex microstructure, the γ -austenite did not decompose. The increased Ni content was expected to increase the decomposition rate of austenite, as observed in the sample with 5.6% Ni, but it did not. The CALPHAD calculations show that the amount of B2 ordered phase is, in fact, severely lowered at 8.6 wt.% Ni. The secondary B2 ordered phase peak during cooling, which is attributed to the austenite decomposition, is much lower than the other compositions. The start temperature of kappa carbide formation is also the lowest and attributed to the absence of kappa carbides. It is interesting to note that Ni is mainly present in the α -ferrite, although it is a gamma-forming element. The SEM EDS mapping results confirm the Thermo-Calc calculations, as can be seen in Figure 11.

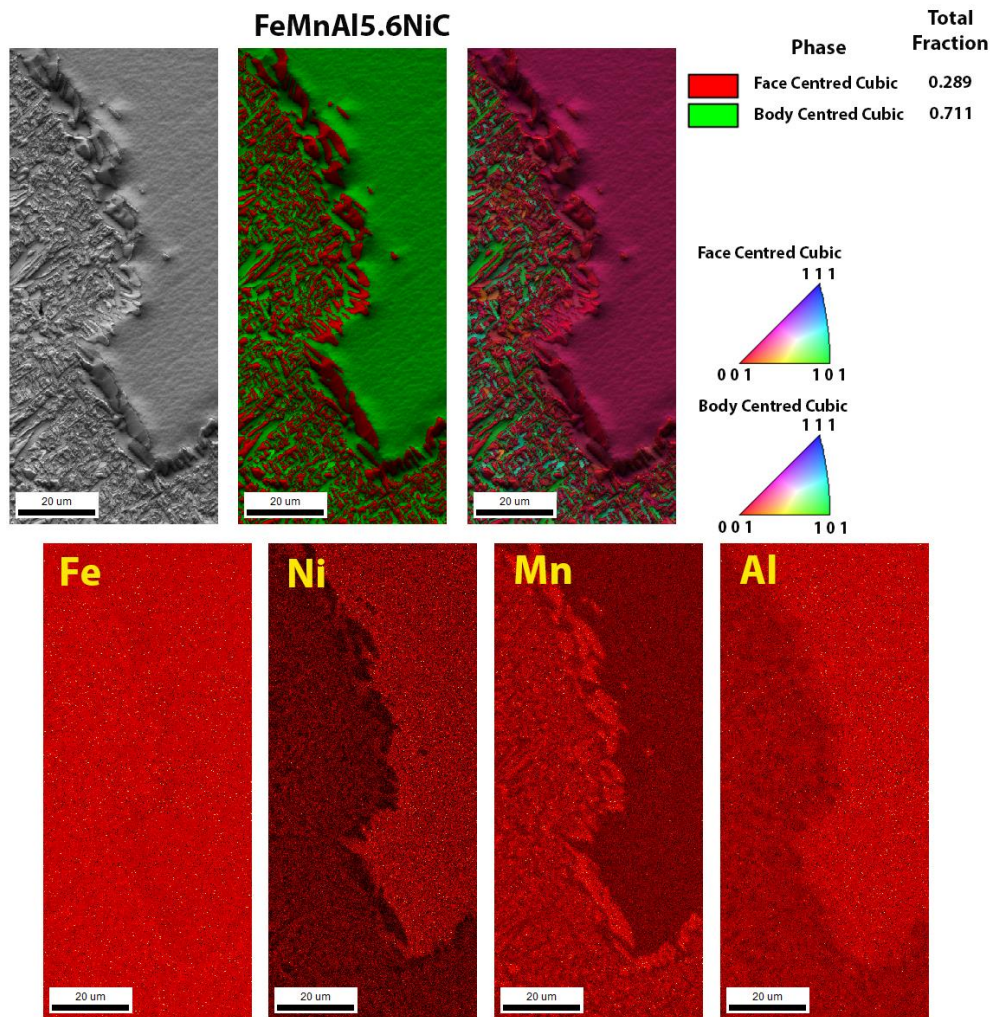


Figure 9. Electron backscattered diffraction analysis of a sample as-cast FeMnAl5.6NiC sample and SEM EDS (Energy-dispersive X-ray spectroscopy) elemental mapping of Fe, Ni, Mn, and Al.

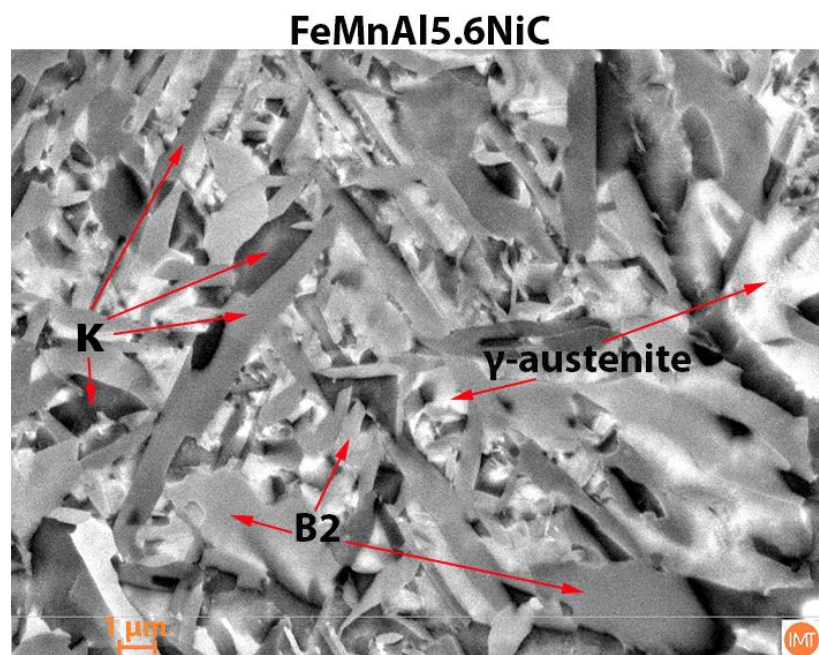


Figure 10. The decomposed austenite consists of kappa carbides, B2 ordered phase and γ -austenite.

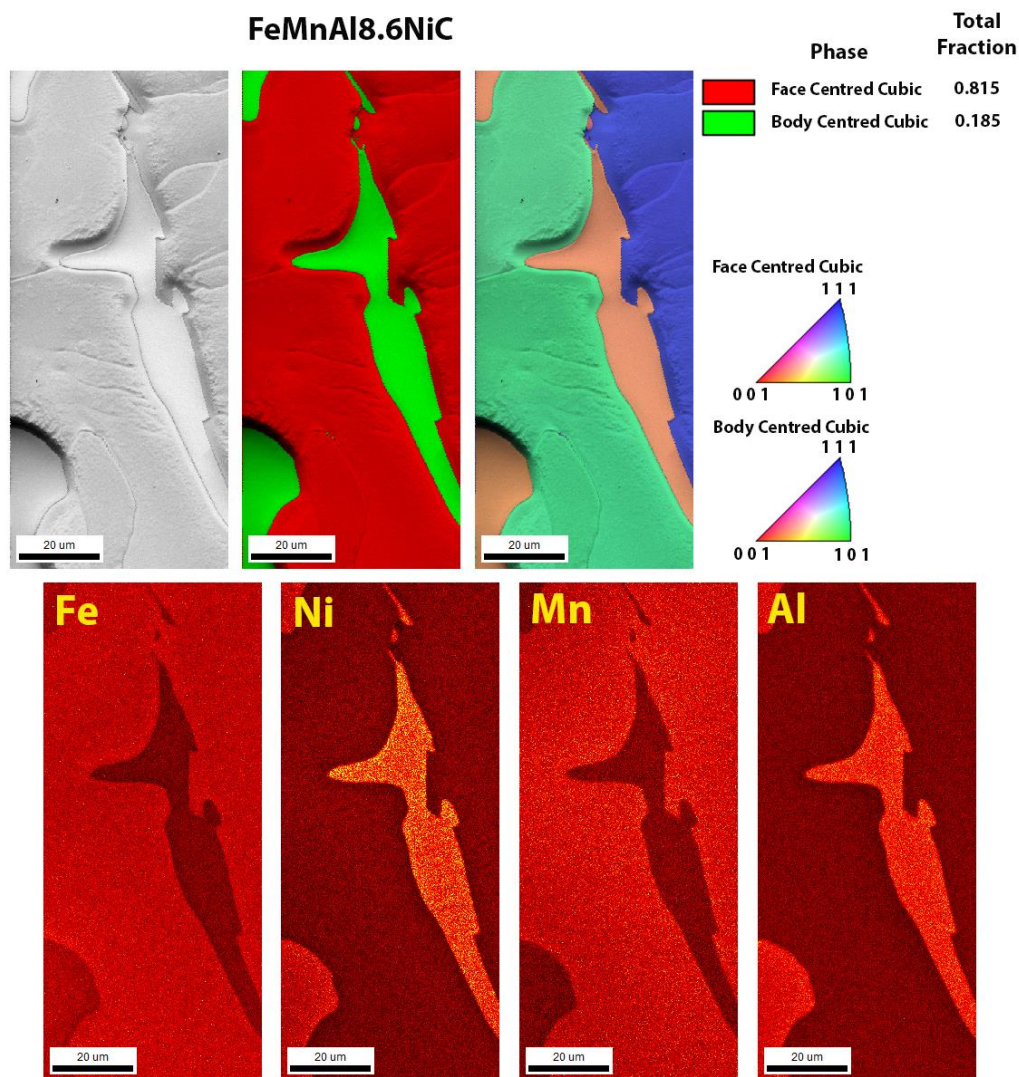


Figure 11. Electron backscattered diffraction analysis of a sample as-cast FeMnAl8.6NiC sample and SEM EDS (Energy-dispersive X-ray spectroscopy) elemental mapping of Fe, Ni, Mn, and Al.

4. Conclusions

The study of the as-cast microstructure of duplex lightweight FeMnAlC steel with various additions of Ni showed that the as-cast microstructure consists of different phases that appear during cooling after solidification. The addition of Ni eliminates the formation of the lamellar kappa carbide and α -ferrite phase that are present in the samples without Ni.

The addition of 1.7 and 3.9 wt.% Ni did not dramatically affect the microstructure besides eliminating the lamellar kappa carbides, but the addition of 5.6 wt.% Ni dramatically affected the decomposition of the gamma phase as it decomposed into kappa carbides, the B2 ordered phase, and γ -austenite. Interestingly, the decomposition of γ -austenite was not observed with the addition of 8.6 wt.% Ni.

Ni is preferentially dissolved in the BCC phase, either in α -ferrite or in the B2 ordered phase.

γ -Austenite undergoes spinodal decomposition, forming coherently ordered kappa carbides. This is most evident in the sample without Ni, while the decomposition of γ -austenite is more subtle at 1.7, 3.9, and 8.6 wt.% Ni, and the ordering of α -ferrite to the B2 ordered phase is also evident.

Author Contributions: Conceptualization and writing, J.B., T.B. and B.Š.B.; original draft preparation, J.B., B.Š.B. and T.B.; methodology and formal analysis, J.B., B.Š.B. and T.B.; validation and formal analysis, J.B. and B.Š.B. All authors have read and agreed to the published version of the manuscript.

Funding: Funding was provided by the Slovenian Research Agency ARRS program P2-0050 (C).

Institutional Review Board Statement: Not applicable.

Informed Consent Statement: Not applicable.

Data Availability Statement: Not applicable.

Conflicts of Interest: The authors declare no conflict of interest.

References

1. Ajanovic, A.; Haas, R. The impact of energy policies in scenarios on GHG emission reduction in passenger car mobility in the EU-15. *Renew. Sustain. Energy Rev.* **2017**, *68*, 1088–1096. [[CrossRef](#)]
2. Lodi, C.; Seitsonen, A.; Pa, E.; De Gennaro, M.; Huld, T.; Malfettani, S. Reducing CO₂ emissions of conventional fuel cars by vehicle photovoltaic roofs. *Transp. Res. Part D Transp. Environ.* **2018**, *59*, 313–324. [[CrossRef](#)]
3. Fontaras, G.; Dilara, P. The evolution of European passenger car characteristics 2000–2010 and its effects on real-world CO₂ emissions and CO₂ reduction policy. *Energy Policy* **2012**, *49*, 719–730. [[CrossRef](#)]
4. Tsiakmakis, S.; Fontaras, G.; Ciuffo, B.; Samaras, Z. A simulation-based methodology for quantifying European passenger car fleet CO₂ emissions. *Appl. Energy* **2017**, *199*, 447–465. [[CrossRef](#)]
5. Hottle, T.; Caffrey, C.; McDonald, J.; Dodder, R. Critical factors affecting life cycle assessments of material choice for vehicle mass reduction. *Transp. Res. Part D Transp. Environ.* **2017**, *56*, 241–257. [[CrossRef](#)]
6. Chen, S.; Rana, R.; Haldar, A.; Ray, R.K. Current state of Fe-Mn-Al-C low density steels. *Prog. Mater. Sci.* **2017**, *89*, 345–391. [[CrossRef](#)]
7. Kim, Y.G.; Kim, T.W.; Han, J.K.; Chang, R.W. Development of New Austenitic Fe-Mn-Al-C Steels for Automotive Applications. *Key Eng. Mater.* **1993**, *84*, 461–471. [[CrossRef](#)]
8. Zuazo, I.; Hallstedt, B.; Lindahl, B.; Selleby, M.; Soler, M.; Etienne, A.; Perlade, A.; Hasenpouth, D.; Cazottes, S.; Kleber, X.; et al. Low-Density Steels: Complex Metallurgy for Automotive Applications. *JOM* **2014**, *66*, 1747–1758. [[CrossRef](#)]
9. Rana, R. Low-Density Steels. *JOM* **2014**, *66*, 1730–1733. [[CrossRef](#)]
10. Kim, H.; Suh, D.; Kim, N.J. Fe–Al–Mn–C lightweight structural alloys: A review on the microstructures and mechanical properties. *Sci. Technol. Adv. Mater.* **2013**, *14*, 014205. [[CrossRef](#)]
11. Howell, R.A.; Van Aken, D.C. A literature review of age hardening Fe-Mn-Al-C alloys. *Iron Steel Technol.* **2009**, *6*, 193–212.
12. Abedi, H.R.; Zarei Hanzaki, A.; Ou, K.L.; Yu, C.H. Substructure hardening in duplex low density steel. *Mater. Des.* **2017**, *116*, 472–480. [[CrossRef](#)]
13. Chen, P.; Li, X.; Yi, H. The κ -carbides in low-density fe-mn-al-c steels: A review on their structure, precipitation and deformation mechanism. *Metals* **2020**, *10*, 1021. [[CrossRef](#)]
14. Frommeyer, G.; Brox, U. Microstructures and Mechanical Properties of High-Strength Fe-Mn-Al-C Light-Weight TRIPLEX Steels. *Steel Res. Int.* **2006**, *77*, 627–633. [[CrossRef](#)]
15. Yoo, J.D.; Park, K.T. Microband-induced plasticity in a high Mn-Al-C light steel. *Mater. Sci. Eng. A* **2008**, *496*, 417–424. [[CrossRef](#)]
16. Chumak, I.; Richter, K.W.; Ipser, H. Isothermal sections in the (Fe, Ni)-rich part of the Fe-Ni-Al phase diagram. *J. Phase Equilib. Diffus.* **2008**, *29*, 300–304. [[CrossRef](#)]
17. Kim, C.; Hong, H.U.; Jang, J.H.; Lee, B.H.; Park, S.J.; Moon, J.; Lee, C.H. Reverse partitioning of Al from κ -carbide to the γ -matrix upon Ni addition and its strengthening effect in Fe–Mn–Al–C lightweight steel. *Mater. Sci. Eng. A* **2021**, *820*, 141563. [[CrossRef](#)]
18. Rahnema, A.; Kotadia, H.; Sridhar, S. Effect of Ni alloying on the microstructural evolution and mechanical properties of two duplex light-weight steels during different annealing temperatures: Experiment and phase-field simulation. *Acta Mater.* **2017**, *132*, 627–643. [[CrossRef](#)]
19. Kim, S.; Kim, H.; Kim, N.J. Brittle intermetallic compound makes ultrastrong low-density steel with large ductility. *Nature* **2015**, *518*, 77–79. [[CrossRef](#)]
20. Park, G.; Nam, C.H.; Zargarani, A.; Kim, N.J. Effect of B2 morphology on the mechanical properties of B2-strengthened lightweight steels. *Scr. Mater.* **2019**, *165*, 68–72. [[CrossRef](#)]
21. Drouven, C.; Song, W.; Bleck, W. Phase-Specific Precipitation of Intermetallic Phases in Fe Al Mn Ni C Duplex Steels. *Steel Res. Int.* **2019**, *90*, 1800440. [[CrossRef](#)]
22. Xu, X.; Cheng, H.; Wu, W.; Liu, Z.; Li, X. Stress corrosion cracking behavior and mechanism of Fe-Mn-Al-C-Ni high specific strength steel in the marine atmospheric environment. *Corros. Sci.* **2021**, *191*, 109760. [[CrossRef](#)]
23. Burja, J.; Šuler, B.; Nagode, A. Effect of ageing temperature on reverse austenite content in AISI 630 stainless steel. *Materwiss. Werksttech.* **2019**, *50*, 405–411. [[CrossRef](#)]
24. Burja, J.; Šuler, B.; Češnjaj, M.; Nagode, A. Effect of intercritical annealing on the microstructure and mechanical properties of 0.1C-13Cr-3Ni martensitic stainless steel. *Metals* **2021**, *11*, 392. [[CrossRef](#)]

25. Andersson, J.O.; Thomas, H.; Lars, H.; Pingfang, S.; Bo, S. Thermo-Calc & DICTRA, computational tools for materials science. *Calphad* **2002**, *26*, 273–312. [[CrossRef](#)]
26. Thermo-Calc AB. *Thermo-Calc Software TCFE10: TCS Steel and Fe-Alloys Database*; Thermo-Calc AB: Solna, Sweden, 2019.
27. Balaško, T.; Burja, J.; Medved, J. Effect of Ni on solidification of duplex low-density steels. *J. Therm. Anal. Calorim.* **2020**, *142*, 1605–1611. [[CrossRef](#)]
28. Mapelli, C.; Barella, S.; Gruttadauria, A.; Mombelli, D.; Bizzozero, M.; Veys, X. γ Decomposition in Fe–Mn–Al–C lightweight steels. *J. Mater. Res. Technol.* **2020**, *9*, 4604–4616. [[CrossRef](#)]
29. Lu, W.J.; Zhang, X.F.; Qin, R.S. κ -carbide hardening in a low-density high-Al high-Mn multiphase steel. *Mater. Lett.* **2015**, *138*, 96–99. [[CrossRef](#)]